Optics Communications 437 (2019) 204–213

Contents lists available at ScienceDirect

Optics Communications

journal homepage: www.elsevier.com/locate/optcom

Misalignment correction for free-form surface in non-null interferometric testing

Zhongming Zang [a], Dong Liu [a], Jian Bai [a,*], Yuhao Zhou [a], Tianliang Yan [a], Sijie Chen [a], Yue Wang [a], Yuling Liu [a], Lei Zhang [a], Tu Shi [a], Wei Huang [b], Liang Miao [b]

[a] State Key Laboratory of Modern Optical Instrumentation, College of Optical Science and Engineering, Zhejiang University, Hangzhou 310027, China

[b] State Key Laboratory of Applied Optics, Changchun Institute of Optics, Fine Mechanics and Physics, Chinese Academy of Sciences, Changchun 130033, China

ARTICLE INFO

Keywords:
Free-form surface
Surface measurement
Figure
Interferometry

ABSTRACT

Unlike rotational symmetric surfaces, free-form surfaces have sophisticated degrees of freedom, therefore, are more difficult to be aligned. In this work, a practical and accurate correction method is proposed for the misalignment removal of the free-form surface in a non-null interferometric testing system based on computer modeling. The misalignment aberrations, introduced by axial location error, rotation error and non-axial attitude error, are modeled and corrected step by step. The axial and non-axial positions of the free-form surface in the computer model are adjusted from the ideal position to the misaligned one, matching the actual positions in experiment for the correction. Since the modeled position are tuned to be consistent with the actual one, all the misalignment aberrations can be removed from the test wavefront with the reconstruction algorithm. Computer simulations are displayed to verify the accuracy of the proposed method. Experimental results after alignment show basic consistency with the results of Taylor Hobson Profilometer, in which the peak-to-valley (PV) value error of the profile line is better than $1/30\lambda$.

1. Introduction

Compared with spherical and aspheric optics, free-form surfaces can provide more degrees of freedom in optical design [1]. Therefore, they are very popular in the field of lighting, display, and imaging, etc. [2]. The fabrication technology for free-form surfaces has made a great progress in recent years. To keep pace with the development of fabrication, a high-precision metrology is needed. Currently, several aspheric and free-form surface testing methods have been proposed, such as using Shack–Hartmann sensor [3], phase measuring deflectometry [4,5], and interferometry [6–11], etc. As one of the most accurate testing methods, interferometry has made great achievements in the testing of free-form surfaces. With the help of special null optics, such as computed generated holograms (CGH) [8], null interferometry can achieve high-precision measurement. However, every test part requires one unique null optics, which strongly reduces the versatility of null interferometry. On the contrary, non-null interferometry such as sub-aperture stitching interferometer (SSI) [10] and tilted-wave-interferometer (TWI) [11], can provide much better versatility. By replacing the standard null compensator with the partial null lens (PNL), the partial compensating interferometer can obtain better versatility and keep high accuracy for the free-form surface test with the retrace error correction algorithms.

In either null or non-null interferometry, the misalignment of the free-form surface has always been one of the most important factors restricting the testing accuracy. The advantage of the null interferometric setup is that the testing results directly show the deviation of the test surface from the standard shape. Slight misalignment between the interferometric setup and the free-form surface under test will produce large aberrations, leading to high fringes density. Subsequently, alignment can be adjusted effectively based on the density of testing interference fringes. For non-null interferometric setup, it allows the introduction of higher fringes density, usually with the additional retrace error correction. However, the residual wavefront aberrations in the test wavefront make it difficult to distinguish the misalignment aberrations from the figure error and retrace error. Hou et al. [12] removed the first four terms from Zernike coefficients of the test wavefront directly and successfully aligned the aspheric under test. Baer et al. [13] proposed a calibration method for the radial and axial displacement of the aspheric based on TWI, which mainly includes the adjustment of the interferometric setup, as well as the coarse and five-dimensional adjustment of the test surface. Li et al. [14] proposed a method for the rotation error controlling of free-form surface in TWI and achieved promising results. These methods tried to adjust the position in the experimental system close to the theoretical one, and achieve relatively high accuracy. Hao et al. [15] proposed an alignment method

* Corresponding author.
E-mail address: bai@zju.edu.cn (J. Bai).

https://doi.org/10.1016/j.optcom.2018.12.023
Received 12 November 2018; Received in revised form 30 November 2018; Accepted 4 December 2018
Available online 18 December 2018
0030-4018/

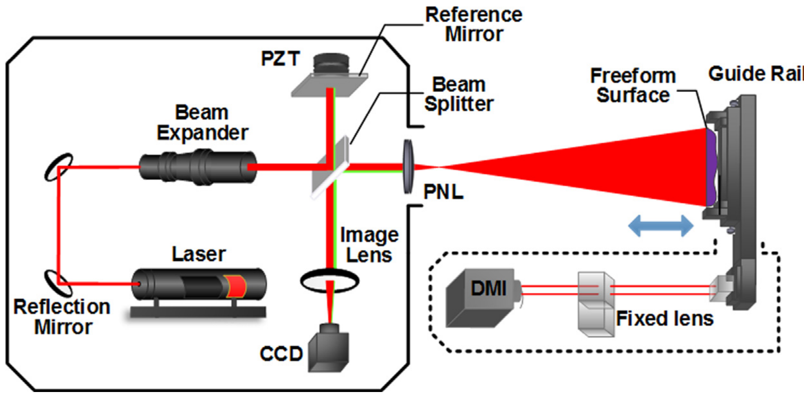

Fig. 1. The sketch of non-null interferometric testing system.

based on computer modeling, which the position parameters of the free-form surface in the model are consistently optimized to match the actual ones in a ray tracing program.

In this paper, a practical and accurate correction method is proposed for the misalignment removal of the free-form surface in a non-null interferometric testing system. Firstly, the computer modeling of interferometric configuration is set up accurately, according to the corresponding parameters of each component in the actual experiment. Then, the misalignment aberrations, introduced by axial location error, rotation error and non-axial attitude error, are modeled and corrected step by step with three specific methods. During the correction, the position of free-form surface in the model is adjusted from the ideal position to the misaligned one, matching that of the actual surface in the experiment. Since the modeled position is consistent with the actual one, the test wavefront in the model is also considered to be consistent with that in the actual experiment. Therefore, the accurate figure error of the free-form surface can be further obtained using the computer reconstruction algorithms. This correction procedure is carried out in the computer modeling, without troublesome alignment for the free-form surface in the experiment. Both computer simulations and experimental results show that the proposed method can correct the misalignment of free-form surface effectively.

In Section 2, a non-null interferometric testing system and the analysis of misalignment are presented. In Section 3, a detailed illustration of the correction method is presented. Simulations, involving the accuracy analysis and the error consideration, is presented in Section 4. In Section 5, experiments are carried out to verify the practical feasibility of the proposed method. Conclusions are summarized in Section 6.

2. Misalignment for free-form surface in non-null interferometric testing system

2.1. Non-null interferometric testing system

A non-null interferometric testing system based on Twyman–Green structure is illustrated in Fig. 1. The laser beam collimated by beam expander is divided into two by the beam splitter. One is reflected by a reference mirror on which a piezoelectric ceramic transducer (PZT) is mounted, serving as the reference beam; the other travels through the PNL, and is then reflected by the free-form surface under test, serving as the test beam after traveling through the PNL again. The PNL, which could be regarded as the part under test in common interferometers, is imaged onto the Charge-coupled Device (CCD) detector, in which the interference fringes are visible. The PZT is used to produce phase shifting between the reference and the test beams. During testing, the free-form surface is moved along the optical axis monitored by the displacement measuring interferometer (DMI) and multiple interferograms are recorded by the CCD. The test wavefront can be further extracted from the interferograms with the phase-shifting

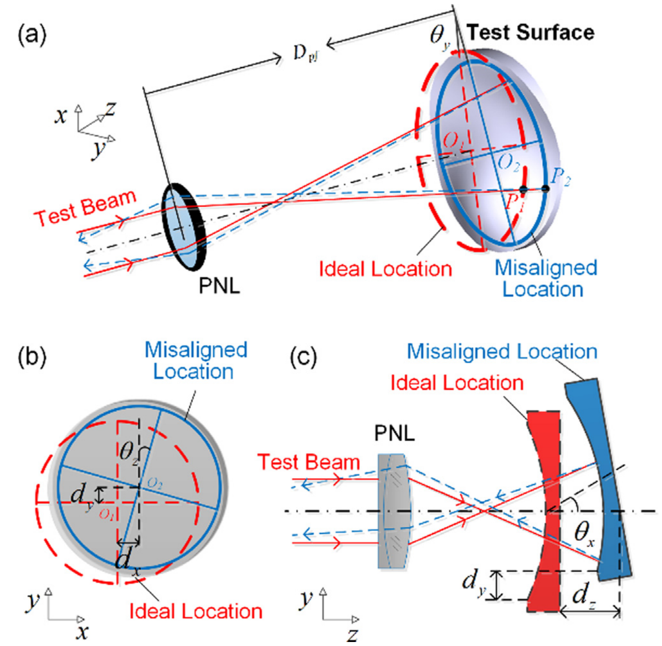

Fig. 2. Schematic diagrams of the free-form surface misalignments. (a) Three-dimensional sketch. (b) Vertical (x-y) cross section. (c) Horizontal (y-z) cross section.

algorithm, which are employed to get the figure error. Meanwhile, the non-null interferometric testing system is modeled in a ray tracing program according to the parameters of actual setup for the figure error reconstruction.

Note that, the testing results of figure error are largely influenced by the retrace error and the aberrations caused by the misalignment of free-form surface. For non-null interferometric system, the PNL is employed to produce an aspheric reference wavefront, which partially compensates the longitudinal normal aberration of the free-form surface. The rays traveling through the PNL, however, may slightly deviate from the normal of the free-form surface under test, which cause the reflected rays to be further separated from the incident ones, leading to the retrace error. In our previous work [16], the computer modeling and reverse optimizing reconstruction (ROR) algorithm is employed for the retrace error correction and accurate figure error reconstruction. However, the ROR procedure requires a high-precision computer modeling. If the test surface is misaligned, the reconstructed results will be largely affected. Therefore, it is important to correct the misalignment of the free-form surface.

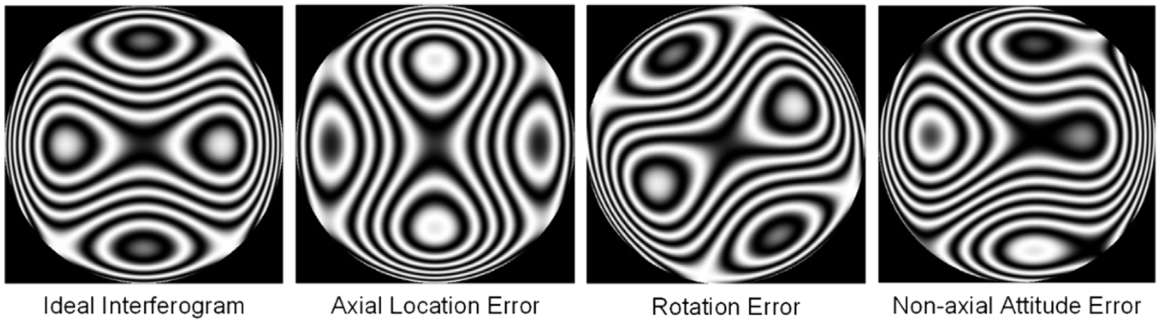

Fig. 3. Interferograms with misalignment.

2.2. Misalignment analysis

In this paper, the misalignment refers to the deviation between the ideal system model and the actual experiment, which are illustrated in Fig. 2. The three-dimensional sketch of a misaligned test surface deviating from the ideal location is exhibited in Fig. 2(a), while the Figs. 2(b) and 2(c) show the vertical (x-y) cross section and horizontal (y-z) cross section, respectively. In 3D Cartesian space, there are six basic misalignments including three translations (d_x, d_y and d_z) and three rotations (θ_x, θ_y and θ_z) about respective axes. Considering the adjustment accuracy of the test surface is limited by the actual system, the test surface is placed as close as possible to the ideal location; then the free-form surface in model is adjusted to actual location to minimize the misalignment.

In this paper, the misalignments, which are shown in Fig. 2, are divided into three categories, namely axial location error, rotation error, and non-axial attitude error, which are corrected sequentially. The interferograms of a biconic surface with different kinds of misalignments are illustrated in Fig. 3. The axial location error refers to the deviation of the absolute position along the optical axis (z axis) direction. For non-null interferometric configuration, the axial displacement of the free-form surface is monitored by the DMI. However, the initial axial location (D_{pf}) between the PNL and the test surface is difficult to be accurately determined, which will directly affect the system modeling accuracy. In this case, other correction methods cannot be precisely applied. Therefore, it is necessary to remove axial location error first. The angular deviation around the optical axis (θ_z) is named rotation error. Since the free-form surface generally do not have rotational symmetric structures, the influence of rotation misalignment should be considered. For practical interferometric setup, it is difficult to obtain the exactly consistency of coordinate between the computer model and the actual experiment. The inconsistency in the rotation direction between the model and the actual experiment causes large rotation error and therefore producing the inconsistency of interferograms at the same position. Considering that the inconsistency of interferograms would influence the correction of the non-axial attitude error, the rotation error must be corrected next. Generally, the non-axial attitude error is the deviation between the symmetric axis of the test surface and that of the interferometer. However, the free-form surface may not have a classical optical axis, making it impossible to determine whether it coincides with the optical axis of the interferometer. In this paper, the non-axial attitude error of the free-form surface refers to position deviations between the system model and the actual experiment other than the axial location error and rotation error, including tilt and decentering around x and y axis (θ_x, θ_y, d_x and d_y) and remaining small amount of defocus (d_z). The non-axial attitude error is corrected at last.

3. Misalignment correction for free-form surface

3.1. Axial location error correction

The axial location error introduces the defocus aberration into the test wavefront, causing the Zernike defocus coefficient of the test wavefront in the actual experiment shifted from the corresponding one in the model. Consequently, when the Zernike defocus coefficient in the model is consistent with that in the actual experiment, the initial axial location in the actual experiment can be aligned to be consistent with the model one. However, for free-form surface, there may be more than one axial location where the Zernike defocus coefficients of the test wavefront are the same due to non-symmetry of surface, which indicates that the axial location cannot be determined by one defocus coefficient alone. Therefore, a continuous axial curve matching method is proposed for the axial location error correction. Fig. 4 illustrates the principle of the proposed method. In the actual experimental system, the free-form surface is continuously placed at different axial locations, whose axial displacement are monitored by the DMI. Extracted from the test wavefronts at different locations, the Zernike defocus coefficients are fitted into a curve, shown as the red solid line. Meanwhile, a longer period of the axial locations is obtained from the computer model and the Zernike defocus coefficients of the corresponding wavefronts are served as target curve, shown as the red dotted line. Searching the overlaps of the fitting curve in the target curve, the initial location is obtained and the axial location error can be aligned to zero when the initial axial location in the model is moved to be consistent with the actual one in the experiment.

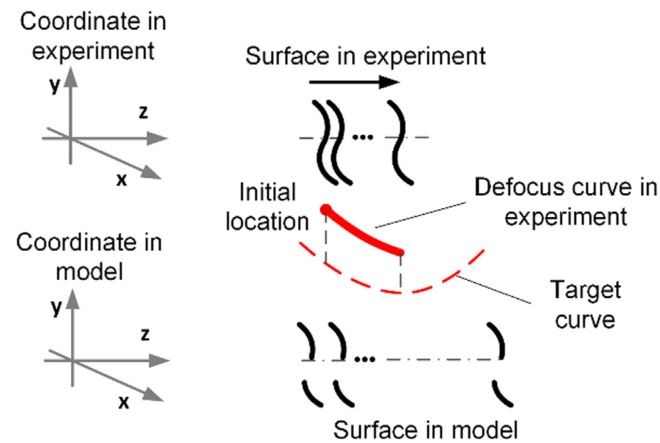

Fig. 4. The principle of continuous axial curve matching method. . (For interpretation of the references to color in this figure legend, the reader is referred to the web version of this article.)

Note that, the accuracy of the axial location solution can be affected, if the free-form surface has slight rotation error or other misalignments. In such case, other aberrations considering the surface features should be also selected as an auxiliary curve to jointly solve the axial location error of the free-form surface in the actual experiment. In addition, if the departure of the free-form surface increases, it would not be able to obtain the resolvable interferogram in the full aperture. It is necessary to calculate the defocus and other aberrations coefficients in an effective

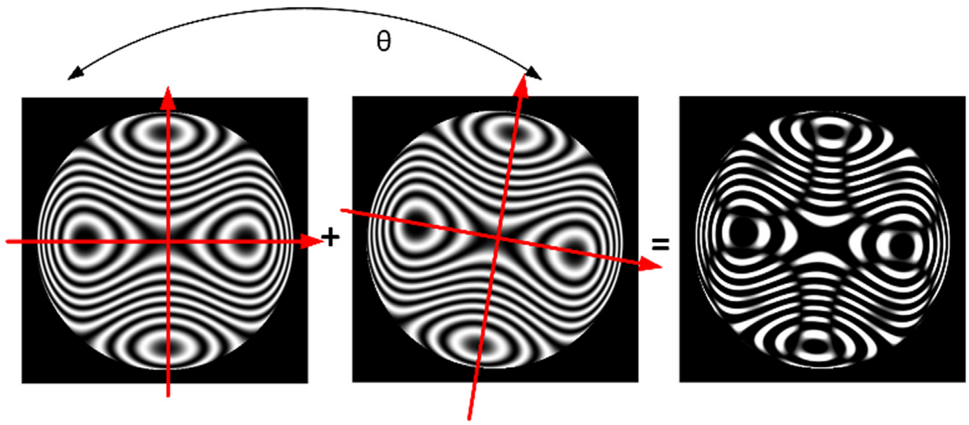

Fig. 5. Moire fringes created by superposition of interferograms with the rotation error.

circular area where fringes are sparse, and then the Zernike coefficients in the full aperture can be obtained by mathematical conversion which is described in detail in Section 3.3.

3.2. Rotation error correction

Moire-fringe technology is applied here to correct the rotation error of the free-form surface between the model and the actual experiment. As shown in Fig. 5, the Moire fringes are produced by superposing the experimental and the model interferograms. The fringe spacing of Moire fringes W can be expressed as

$$W = \frac{d}{\theta}, \tag{1}$$

where d is the spacing of the interference fringes, while θ is the relative angle caused by the rotation error between the two interferograms. Eq. (1) illustrates that the introduction of Moire fringes is related to the rotation error angle θ of the free-form surface between the model and the experiment. If the rotation error angle θ becomes smaller, the fringe spacing W increases and therefore decreases the number of Moire fringes in the interferogram. In this case, the rotation error ought to be corrected to zero with the disappearing of the Moire fringes. In practical testing, usually a precise mechanical rotation stage is employed to control the rotation angle of the free-form surface in the experimental configuration, but it is still difficult to manually adjust the rotation angle to be consistent with that of the model. However, it is relatively easy and more accurate to adjust the rotation angle of the free-form surface in the model system. This procedure can be described as: if the Moire fringes are created by superposing the model and the experimental interferograms, it means that the rotation error exists in the test surface between the model and the actual experiment. Then, revision of the rotation angle should be carried out in the model to match the actual rotation of the free-form surface in the experiment, until the Moire fringes disappear.

3.3. Non-axial attitude error correction

The aberrations of the test wavefront due to non-axial attitude error has been discussed in detail [17]. It is evident that some low-order aberrations (tilt, defocus and coma) coefficients would be enough to correct non-axial attitude error. In addition, the other aberrations may be attributed to the combination of misalignment, retrace error and figure error, which cannot be used for misalignment correction.

A correction model is proposed in previous work [18] for rotational symmetric aspherics. In the previous work, the misalignment coefficients of annular sub-apertures are employed to calculate the corresponding full aperture misalignment due to the limited resolution. The specific misalignment of the test surface is revised in the model to be consistent with the actual one according to the acquired full

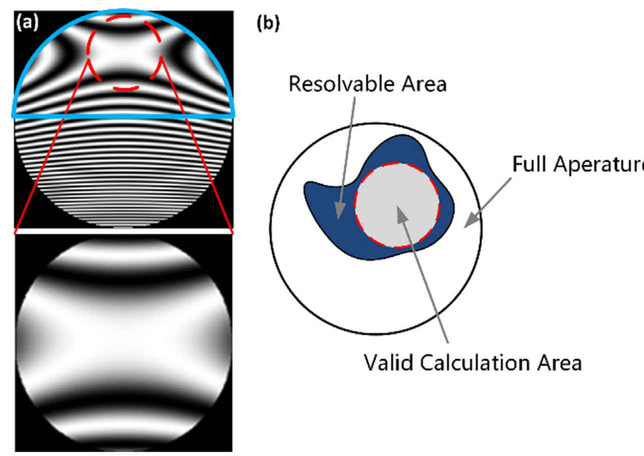

Fig. 6. Valid calculation area (VCA). (a) the interferogram of free-form surface, (b) the choice of VCA. . (For interpretation of the references to color in this figure legend, the reader is referred to the web version of this article.)

aperture misalignment coefficients. However, this procedure cannot be employed effectively to the free-form surface testing because the resolvable interferogram of the free-form surface may have irregular aperture shape, as illustrated in Fig. 6(a). Only top half circular area at the full aperture is resolvable and can be detected by the CCD, shown as the blue area. To be noted, the test wavefront in the resolvable area is fitted with Zernike coefficients and the non-axial attitude error coefficients are obtained. We choose a circular area from the resolvable area, serving as the valid calculation area (VCA) to calculate the non-axial attitude error of the full aperture, as shown in Fig. 6(b). The specific conversion between the VCA and the full aperture is indicated below.

Fig. 7(a) shows the normalized aperture of the VCA, where the normalized coordinate of the point A is (ρ', θ'). Fig. 7(b) shows the normalized aperture of the full aperture, where the normalized coordinate of the same point A is (ρ, θ).

Since the rotation error has been corrected, the misalignment aberrations introduced by the non-axial attitude error of the random point A, which are consistent in the VCA and the full aperture, can be expressed as the sum of tilt, coma and defocus as follows

$$\begin{aligned} &\mathrm{W}_{\mathrm{defocus}}(\rho,\theta) + \mathrm{W}_{\mathrm{tilt}}(\rho,\theta) + \mathrm{W}_{\mathrm{coma}}(\rho,\theta) \\ &= \mathrm{W}_{\mathrm{defocus}}(\rho',\theta') + \mathrm{W}_{\mathrm{tilt}}(\rho',\theta') + \mathrm{W}_{\mathrm{coma}}(\rho',\theta'). \end{aligned} \tag{2}$$

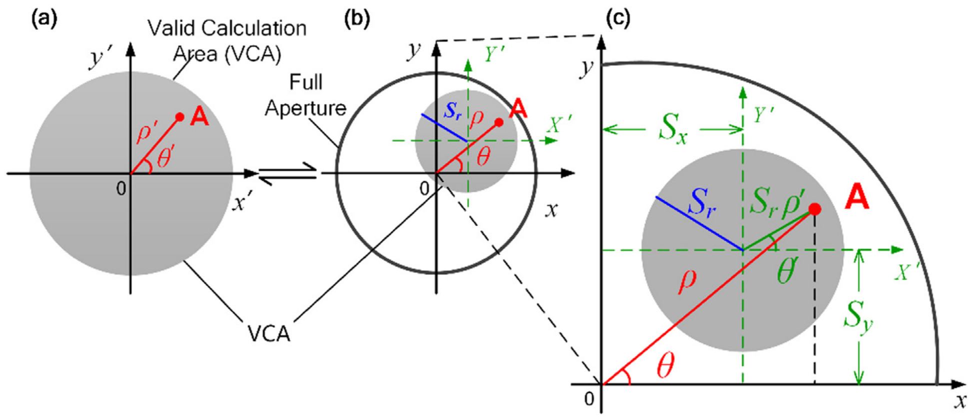

Fig. 7. Coordinate conversion, (a) VCA, (b) full aperture, (c) coordinate conversion.

The misalignment aberrations in Eq. (2) can be expanded into standard Zernike polynomials, and the Eq. (2) can be expressed as

$$\begin{cases} 2C_2\cos\theta + \sqrt{8}C_8(3\rho^3 - 2\rho)\cos\theta = 2C_{s2}\cos\theta' + \sqrt{8}C_{s8}(3\rho'^3 - 2\rho')\cos\theta' \\ 2C_3\sin\theta + \sqrt{8}C_7(3\rho^3 - 2\rho)\sin\theta = 2C_{s3}\sin\theta' + \sqrt{8}C_{s7}(3\rho'^3 - 2\rho')\sin\theta' \\ C_4 \cdot S_r^2 = C_{s4} \end{cases}, \tag{3}$$

where C_2 and C_3 are x tilt and y tilt coefficients, C_7 and C_8 are x coma and y coma coefficients, C_4 is defocus coefficient of the test wavefront in the full aperture, and C_{s2}, C_{s3}, C_{s4}, C_{s7} and C_{s8} are to the corresponding ones in the VCA. The coordinate conversion as shown in Fig. 7(c) can be expressed as

$$\begin{cases} \cos\theta = \dfrac{S_x + S_r\rho'\cos\theta'}{\left[\left(S_x + S_r\rho'\cos\theta'\right)^2 + \left(S_y + S_r\rho'\sin\theta'\right)^2\right]^{1/2}} \\ \sin\theta = \dfrac{S_y + S_r\rho'\cos\theta'}{\left[\left(S_x + S_r\rho'\cos\theta'\right)^2 + \left(S_y + S_r\rho'\sin\theta'\right)^2\right]^{1/2}} \\ \rho = \left[\left(S_x + S_r\rho'\cos\theta'\right)^2 + \left(S_y + S_r\rho'\sin\theta'\right)^2\right]^{1/2} \end{cases}, \tag{4}$$

where (S_x, S_y) is the normalized coordinate of the VCA in the full aperture, and S_r is the ratio of radius between the full aperture and the VCA. These three parameters can be easily obtained from the interferogram. From Eqs. (2)–(4) we can obtain

$$\begin{cases} C_2 = C_{s2}\cdot\left(1/S_r\right) + C_{s8}\cdot\sqrt{8}\left(1/S_r^3 - 1/S_r - P\right) \\ C_3 = C_{s3}\cdot\left(1/S_r\right) + C_{s7}\cdot\sqrt{8}\left(1/S_r^3 - 1/S_r - Q\right) \\ C_4 \approx C_{s4}\cdot\left(1/S_r^2\right) - T \\ C_7 = C_{s7}\cdot\left(1/S_r^3\right) \\ C_8 = C_{s8}\cdot\left(1/S_r^3\right) \end{cases}, \tag{5}$$

where P, Q, T are expressed as

$$\begin{cases} P = \dfrac{\left[3\left(S_x^2 + S_y^2\right)/2 + 3S_x\left(S_x + S_y\right) + C_{s4}S_x/C_8' S_r^2\right]}{S_r^3} \\ Q = \dfrac{\left[3\left(S_x^2 + S_y^2\right)/2 + 3S_y\left(S_x + S_y\right) + C_{s4}S_y/C_{s7} S_r^2\right]}{S_r^3} \\ T = \dfrac{\sqrt{6}\left(C_{s8}S_x + C_{s7}S_y\right)}{S_r^4} \end{cases}. \tag{6}$$

Eqs. (5) and (6) provide the conversion of non-axial attitude error coefficients between the VCA and the full aperture. Firstly, the non-axial attitude error coefficients of the full aperture are obtained from the corresponding ones of the VCA. Then, the specific misalignment of the full aperture is corrected in the computer model, making the modeled position consistent with the actual experimental one. This method of correcting the position of the test surface in the model, was proposed in our previous work [17].

In addition, the usage of VCA has two advantages. On the one hand, the VCA is easy to be located in the circular full aperture, while the corresponding Zernike coefficients are also easy to be converted. On the other hand, the standard Zernike coefficients in the VCA are still corresponding to Seidel aberrations, which is facilitate to describe the misalignment.

3.4. Procedure of free-form surface misalignment correction

The specific procedure of the free-form surface misalignment correction is as follows:

(a) Set up the theoretical model in a ray tracing program according to the parameters of the experimental system.

(b) Move the test surface as close as possible to the ideal location in model. Collect multiple interferograms from CCD detector and fit the test wavefront with Zernike polynomials.

(c) Search the initial axial location with the method of continuous axial curve matching, and set the initial axial location in the model to be consistent with the actual one in the experiment

(d) Superpose the interferograms of the model and the experiment, and adjust the rotation angle in the model based on the Moire fringes.

(e) Choose a suitable VCA from the actual interferogram in the experiment, and get its non-axial attitude error coefficients (C_{s2}, C_{s3}, C_{s4}, C_{s7}, C_{s8}).

(f) Calculate the non-axial attitude error coefficients of the full aperture (C_2, C_3, C_4, C_7, C_8) according to the corresponding ones of the VCA.

(g) Revise the attitude of the test surface in the model according to the results of (f), until it is consistent with the actual one in the experiment.

It is important to note that, the calculation of the figure error of the free-form surface is based on a high-precision modeling of the experimental system. With the proposed correction method, the axial and non-axial position of free-form surface in the model is adjusted from the ideal position to the misaligned one, matching that of the actual surface in the experiment. All the misalignment aberrations are further removed from the test wavefront by the ROR algorithm and accurate figure error can be obtained. This correction is carried out in the computer modeling, without troublesome alignment for the actual surface in the experiment.

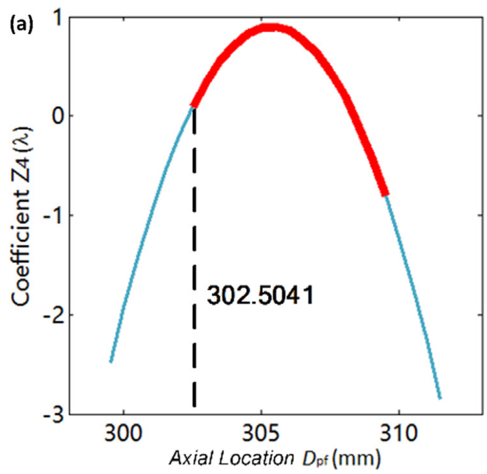

Fig. 8. The axial position error correction, (a) Zernike defocus coefficients, (b) Zernike astigmatism coefficients. . (For interpretation of the references to color in this figure legend, the reader is referred to the web version of this article.)

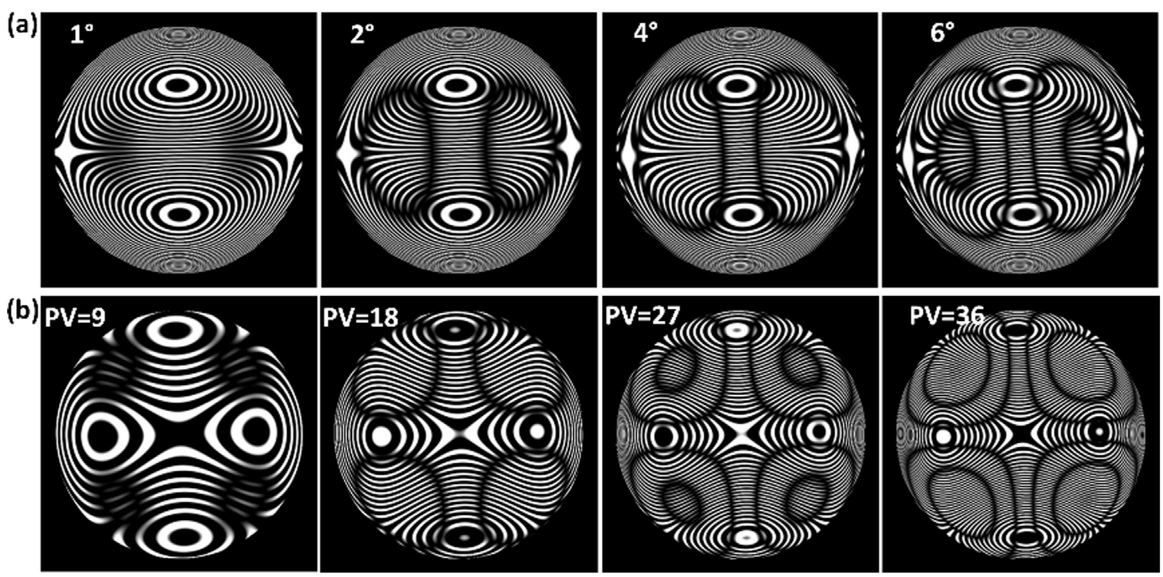

Fig. 9. The axial position error correction, (a) Zernike defocus coefficients, (b) Zernike astigmatism coefficients. . (For interpretation of the references to color in this figure legend, the reader is referred to the web version of this article.)

4. Simulation analyses

To validate the proposed correction method, a biconic surface is simulated in the ray tracing program and the performance of the proposed method is tested. In addition, the error of each method is analyzed separately.

The axial location error is corrected by the curve of Zernike defocus coefficients. However, the defocus aberration of the test wavefront may be affected by the modeling error of the interferometric setup, i.e. figure error, thickness, refractive index and radius of curvature of each component, which need to be considered in practice. Under this consideration, the Zernike defocus coefficient (Z_4) of the test wavefronts at different locations both in the ideal model and simulated experiment are fitted as curves, shown as the blue line and red one in Fig. 8(a). However, there are two axial locations corresponding to a same Zernike defocus coefficient, which might mislead the correction. Since the test surface have large astigmatism, the curve of Zernike astigmatism coefficient (Z_6) is also selected as an auxiliary to assist the alignment, as shown in Fig. 8(b). The Zernike defocus coefficient (Z_4) is given a greater weight considering that the defocus aberration is more easily limited during fabrication. By searching the overlaps of the curves, the initial axial location (D_{pf}) of the test surface can be located at 302.5041 mm, with the accuracy better than 0.005 mm (design value is 302.5 mm).

The correction accuracy of the rotation error largely depends on the discernibility of the Moire fringes. Fig. 9(a) illustrates a series of Moire fringes with different rotation error, created by superposing interferograms obtained from the ideal model and the simulated experimental system. It can be seen that the rotation errors are 1 deg, 2 deg, 4 deg, and 6 deg with the same 27 fringes, respectively. Fig. 9(b) shows the Moire fringes with different PV values of 9λ (632.8 nm), 18λ, 27λ and 36λ with the same rotation error of 2 deg. We could find that the Moire fringes decrease with the decrease of the rotation error. In this way, the rotation error can be easily controlled within 1 deg, so that the PV value deviation of figure error obtained by the ROR algorithm is better than 0.1λ while the root-mean-square (RMS) value deviation is better than 0.01λ, compared to when there is no rotation error. Furthermore, the greater departure of the free-form surface is, the denser the interference

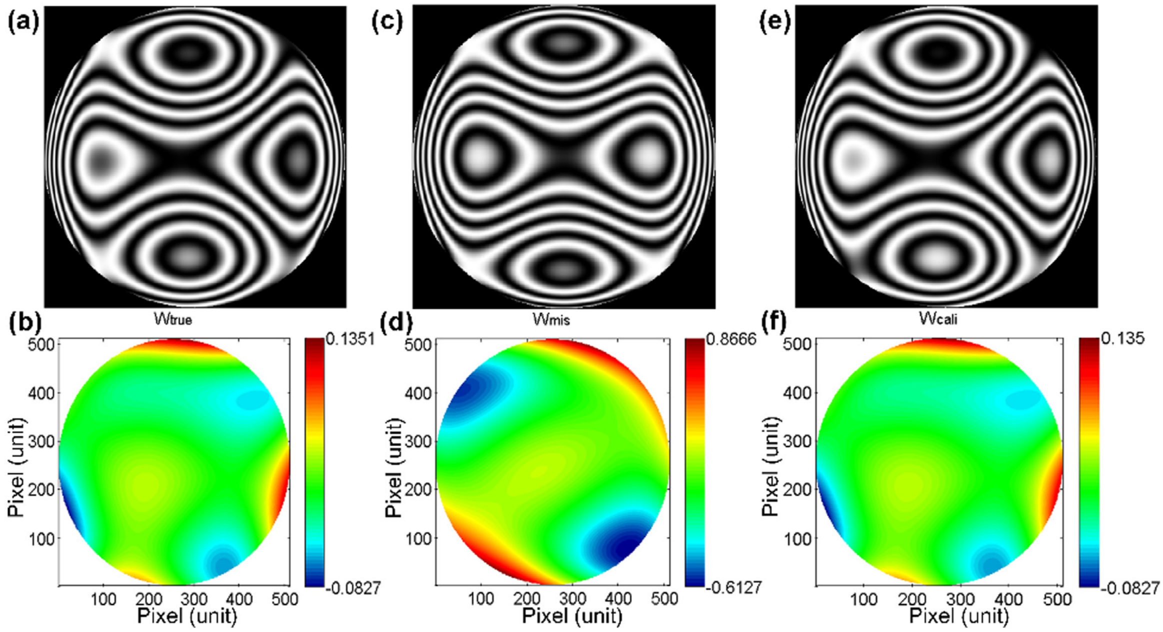

Fig. 10. Interferogram and reconstructed figure error. (a) Simulated experimental interferogram, (b) true figure error, (c) interferogram in model before alignment, (d) reconstructed figure error by (c) with ROR, (e) interferogram in model after alignment, (f) reconstructed figure error by (e) with ROR.

Table 1
Parameter of non-axial attitude error.

d_x (mm)	d_y (mm)	$D_{pf}+d_z$ (mm)	θ_x (deg)	θ_y (deg)
0.0013	0.0013	$301.65+0.03$	−0.0005	−0.0002

Table 2
Parameter of PNL.

Surface	Radius (mm)	Thickness (mm)	Glass (N_d, V_d)	Conic (uint)
1	89.15	10.65	1.52, 64.28	0
2	−50.68			0

fringes are, and there will be more Moire fringes at the same rotation error, which means using this method to correct the rotation error can achieve higher precision.

The method described in Section 3.3 is employed here to correct the non-axial attitude error. The simulated experimental interferogram of test surface with non-axial attitude error is illustrated in Fig. 10(a), and the additive errors are listed in Table 1. If the position of the computer model is exactly same as the actual one, the true figure error of the full aperture can be reconstructed by ROR, as shown in Fig. 10(b). Figs. 10(c) and 10(d) exhibit the interferogram and reconstructed figure error when the model is in the ideal location without misalignment correction. It can be seen that the true figure error is seriously obscured due to the presence of the non-axial attitude error. The non-axial attitude error coefficients are further obtained from Fig. 10(a), and are employed to adjust the model position. Fig. 10(e) illustrates the interferogram in the model after the alignment, which is almost consistent with the actual one. Subsequently, the figure error reconstructed from it with the same algorithm is also basically consistent with the real one, shown in Fig. 10(f). The PV value error is $7.862\times10^{-5}\lambda$ and the RMS value error is $1.107\times10^{-5}\lambda$. With the help of the correction method, the modeled position is adjusted to be consistent with the actual one, and therefore the reconstructed figure error would be credible and accurate.

5. Experimental verification

Experiments were carried out in a testing system as shown in Fig. 1 to verify the practical feasibility of the proposed correction method, in which a biconic surface with an aperture of 20 mm was tested. The nominal shape of biconic surface is

$$z=\frac{\frac{1}{R_x}x^2+\frac{1}{R_y}y^2}{1+\sqrt{1-(1+k_x)\frac{x^2}{R_x^2}-(1+k_y)\frac{y^2}{R_y^2}}}, \tag{7}$$

where $R_x = 242$ mm and $R_y = 238$ mm are the vertex radius of curvature in x and y direction, $k_x = -1.2$ and $k_y = -0.8$ are the conic coefficients in x and y direction, respectively. The test wavelength of the interferometer is 632.8 nm. The PNL is a single lens and the parameters are listed in Table 2. The measurement range of DMI is 40 m, with the precision of $\pm0.5\times10^{-3}$ mm.S

Firstly, the non-null interferometric testing system was modeled in a ray tracing program according to the parameters of the experimental system. With the help of commercial measurement instruments, the figure error of the PNL and other mirrors could be better than 0.05λ (PV), which was almost negligible [17]. The measurement accuracy of refractive index, thickness, and radius of curvature of each component were also better than $\pm10^{-5}$, 5 μm and 0.005%, respectively [19], which made sure the model was consistent with the actual system.

Secondly, the biconic surface under test was moved along the optical axis and multiple interferograms at different locations were detected by the CCD. With the phase-shifting algorithm, a series of actual test wavefronts were obtained and then fitted with Zernike polynomials. The locations obtained by DMI and the corresponding Zernike defocus coefficients were collected for fitting curve, as the red line shown in Fig. 11. Meanwhile, the Zernike defocus coefficients of the test wavefront in the model were obtained with a longer period of locations from 301 mm to 302 mm, served as the target curve shown as the blue line. By matching the two curves, the initial axial location (D_{pf}) of the biconic in the actual experimental system was located at 301.087 mm.

The test surface was moved to 301.087 mm both in the experiment and the model, then the rotation error should be corrected. Fig. 12(a) shows the experimental interferogram at the above location. In order to prevent the influence of noise, the phase was demodulated by phase-shifting algorithm and reconstruct into Fig. 12(b). In the computer model, the interferogram of the test surface at the same location was obtained, as illustrated in Fig. 12(c). By superposing the interferograms

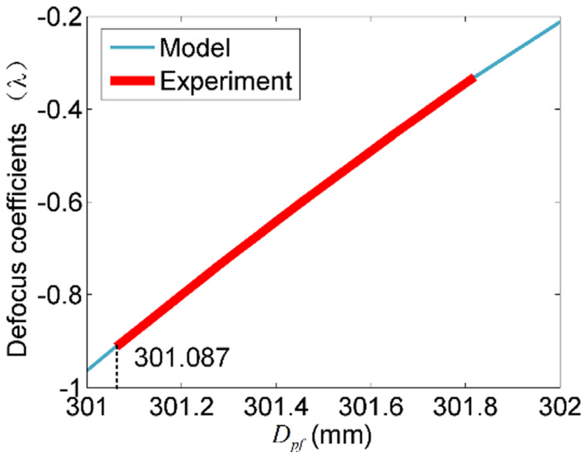

Fig. 11. Fitting curve and target curve of Zernike defocus coefficients. . (For interpretation of the references to color in this figure legend, the reader is referred to the web version of this article.)

of the model and the experiment, six Moire fringes were created (see Fig. 12(d)), which indicated the existence of the rotation error between the experiment and the model. Therefore, relatively revision of the rotation angle was carried out in the model. The test surface in the model was rotated by 5.4 deg clockwise and therefore two Moire fringes were obtained in the superposed interferogram, as shown in Figs. 12(e) and 12(f). The result was the basically consistent with the actual experiment. In this case, the rotation angle of the test surface was kept unchanged both in the model and the experiment.

After the axial error correction, the non-axial attitude error would be corrected. The test surface in the experiment was moved along the optical axis until the interferogram with sparse fringes was obtained, as illustrated in Fig. 13(a). Meanwhile, a similar interferogram at the same location in the model was obtained, as shown in Fig. 13(b). It can be seen that the interferogram in the model was different with the actual one in the experiment, which was largely caused by the figure error and the non-axial attitude error. A circular VCA was selected from the resolvable aperture, to calculate the non-axial attitude error coefficients of the full aperture, shown as the red area. The non-axial attitude error coefficients of VCA both in the model and the experiment are listed in Table 3.

Fig. 14(a) illustrates the non-axial attitude error coefficients displayed in Table 3. According to the conversion between the VCA and the full aperture, the non-axial attitude error coefficients of full aperture were calculated from the corresponding ones in VCA, and the position of the test surface was further revised in the model according to the results. Fig. 14(b) indicates the non-axial attitude error coefficients of VCA in the model after correction, which was basically consistent with the corresponding ones in the experiment. Since the modeled position was consistent with the experimental one, it can be considered that all the misalignments of the biconic surface have been corrected.

Finally, we obtained the figure error of the full aperture by the ROR algorithm, and the two-dimensional (2D) surface map is shown in Fig. 15(b). The PV value of the figure error is 0.8981λ and the RMS value is 0.1841λ. In comparison, the biconic surface is tested with traditional alignment method [20], which provided merely retrace error correction and calibration for misalignment by removing the first four terms from Zernike coefficients of the test wavefront. The 2D surface map of the figure error is presented in Fig. 15(a). The PV value is 0.7672λ and the RMS value is 0.1380λ. In order to verify the accuracy of the measurement results by the proposed method, a 1D profile line was tested with Taylor Hobson profilometer (Form Talysurf i120, 16 nm vertical resolution) [21]. The blue line in Fig. 15(c) shows the profile deviation obtained from the Taylor Hobson, which means the testing results of profilometer subtract the nominal ones. Since the Taylor Hobson measures the roughness, the result is preprocessed by a smooth filter. Meanwhile, the profile deviations at the same position are extracted from Figs. 15(a) and 15(b), as the green line and the red line shown in Fig. 15(c).

Table 4 provides specific PV and RMS value of the profile deviations in Fig. 15(c). The PV and RMS value of the proposed method are 0.5808λ and 0.1718λ, respectively. Compared with the results from profilometer, the PV value error is better than 1/30λ, while the RMS value error is better than 1/36λ. It can be seen in Fig. 15(c) that the profile deviation of the test surface with the proposed method has a better agreement with the one obtained by the profilometer, and the PV difference of the profile between the two method is 1/5λ, while the RMS deviation is 1/20λ. However, the surface map obtained by traditional alignment

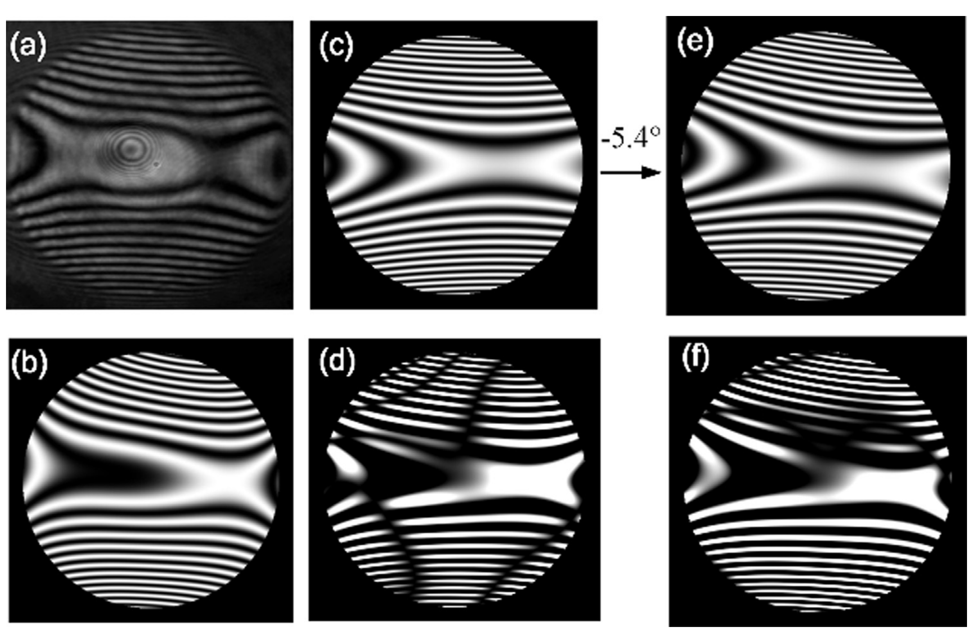

Fig. 12. Correction of the rotation error, (a) experimental interferogram, (b) reconstructed interferogram, (c) original interferogram in the model, (d) Moire fringes by superimposing (b) and (c), (e) revised interferogram, (f) Moire fringes by superimposing (b) and (e).

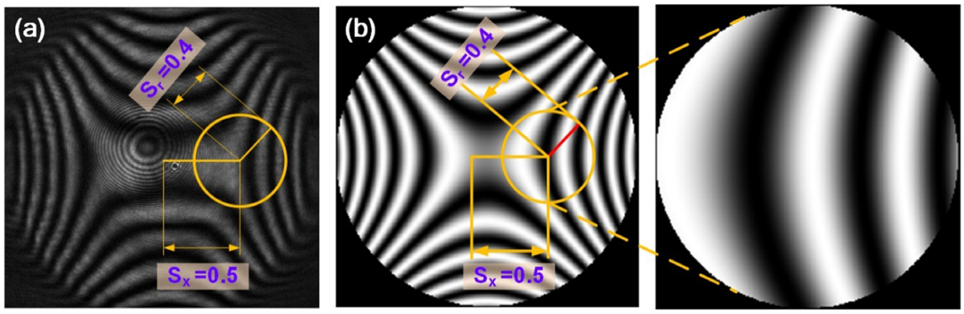

Fig. 13. The choice of VCA, (a) interferogram in the experiment, (b) interferogram in the model. . (For interpretation of the references to color in this figure legend, the reader is referred to the web version of this article.)

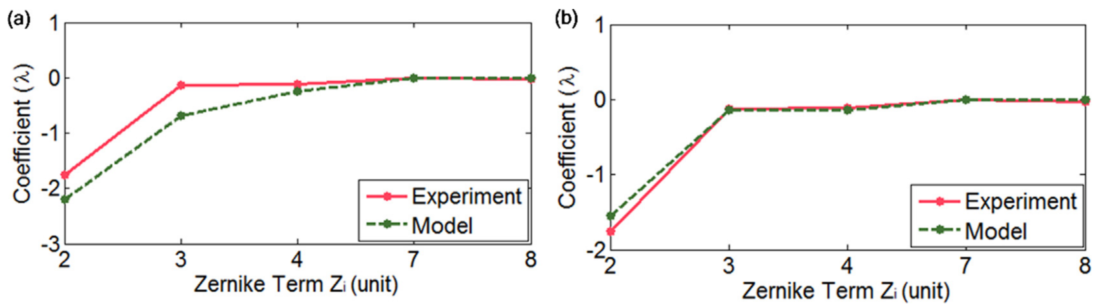

Fig. 14. Comparison of the non-axial attitude error coefficients of VCA, (a) before correction, (b) after correction.

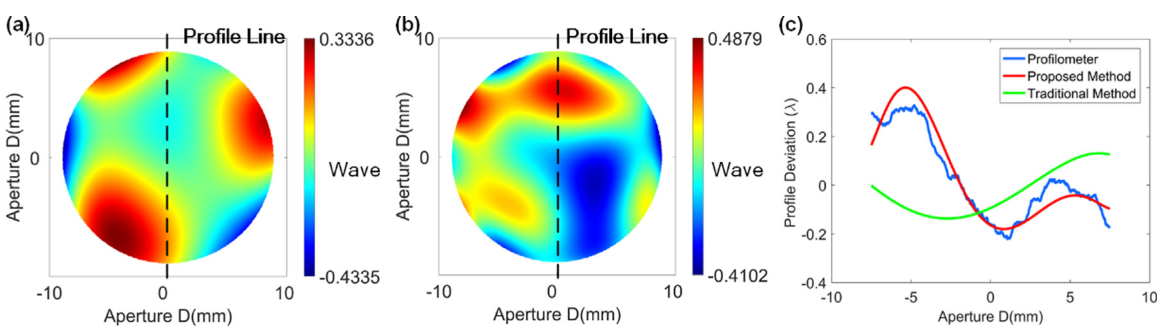

Fig. 15. The experimental results, (a) the figure error with traditional alignment method, (b) the figure error with proposed alignment method, (b) comparison between these two methods and the results from profilometer. . (For interpretation of the references to color in this figure legend, the reader is referred to the web version of this article.)

Table 3
The non-axial attitude error coefficients of VCA in the experiment and the model.

	Z2 (λ)	Z3 (λ)	Z4 (λ)	Z7 (λ)	Z8 (λ)
Experiment	−1.761	−1.282e−1	−1.070e−1	−6.635e−3	−2.671e−2
Model	−2.194	−6.780e−1	−2.473e−1	2.016e−15	3.567e−4

Table 4
PV and RMS values of the profile deviation corresponding to Fig. 15(c).

	PV (λ)	RMS (λ)
Profilometer	0.5487	0.1718
Traditional method	0.2677	0.0975
Proposed method	0.5808	0.1995

method, shown in Fig. 15(a), contain residual high-order misalignment aberrations obscuring the true figure error. Consequently, the profile is completely incapable of matching the profilometer result.

It should be note that, the Taylor Hobson profilometer measures the 1D profile of the biconic surface with limited coverage at one time, while the non-null interferometer equipped with the proposed method has more advantages in directly obtaining the 2D maps of figure error. Although we tried to mark the position of tested profile line on the test surface, it is still difficult to get the profile at the same position for the comparison. Furthermore, the high frequency part of figure error is also difficult to be obtain by interferometer. In this case, the test results may subject to the slight inconsistency of the tested profile position.

6. Conclusion

A practical and accurate misalignment correction method is proposed for the free-form surface in a non-null interferometric testing system. Based on computer modeling, the misalignment aberrations, introduced by the axial location error, rotation error and non-axial position error are modeled and corrected in a ray tracing program. With the proposed method, the axial and non-axial position in the model is adjusted to match that of the actual surface in the experiment. Because only one valid calculation area with resolvable fringes is required, this method can be easily applied to the free-form surface with great departure. Considering the modeled position is consistent with the experimental one, the test wavefronts in the model are also consistent with that in the experiment. All the misalignment aberrations are removed from the test wavefronts and the accurate figure error of the free-form surface is obtained by the ROR algorithm. Note that, since free-from surface is asymmetric, the surface with great departure could be calculated using irregular subaperture stitching, which is also our future works. This correction method depends on the accuracy of system modeling, which avoids the mechanical adjustment or artificial operation in the actual setup.

Acknowledgments

This work was partially supported by the National Key Research and Development Program of China [2016YFC0200700, 2016YFC1400900]; the National Natural Science Foundation of China [61475141]; and the State Key Laboratory of Applied Optics open funds, China.

References

[1] Y. Luo, Z. Feng, Y. Han, H. Li, Design of compact and smooth free-form optical system with uniform illuminance for LED source, Opt. Express 18 (2010) 9055–9063.
[2] X. Jiang, P. Scott, D. Whitehouse, Freeform surface characterisation - a fresh strategy, CIRP Ann. 56 (2007) 553–556.
[3] T.M. Jeong, M. Menon, G. Yoon, Measurement of wave-front aberration in soft contact lenses by use of a Shack–Hartmann wave-front sensor, Appl. Opt. 44 (2005) 4523–4527.
[4] Z. Wang, H. Du, S. Park, H. Xie, Three-dimensional shape measurement with a fast and accurate approach, Appl. Opt. 48 (2009) 1052–1061.
[5] Y.-L. Xiao, J. Xue, X. Su, Robust self-calibration three-dimensional shape measurement in fringe-projection photogrammetry, Opt. Lett. 38 (2013) 694–696.
[6] Y.-S. Ghim, H.-G. Rhee, A. Davies, H.-S. Yang, Y.-W. Lee, 3D surface mapping of freeform optics using wavelength scanning lateral shearing interferometry, Opt. Express 22 (2014) 5098–5105.
[7] L. Yan, X. Wang, L. Zheng, F. Di, F. Zhang, D. Xue, H. Hu, X. Zeng, X. Zhang, Non-null testing for standard quadric surfaces with subaperture stitching technique, Opt. Commun. 340 (2015) 159–164.
[8] P. Su, J. Ma, Q. Tan, G. Jin, G. Kang, Y. Liu, Computer generated hologram null test of a freeform optical surface with rectangular aperture, Opt. Eng. 51 (2012) 025801.
[9] S. Chen, S. Li, Y. Dai, L. Ding, S. Zeng, Experimental study on subaperture testing with iterative stitching algorithm, Opt. Express 16 (2008) 4760–4765.
[10] K.K. Pant, D.R. Burada, M. Bichra, M.P. Singh, A. Ghosh, G.S. Khan, S. Sinzinger, C. Shakher, Subaperture stitching for measurement of freeform wavefront, Appl. Opt. 54 (2015) 10022–10028.
[11] G. Baer, J. Schindler, C. Pruss, J. Siepmann, W. Osten, Fast and flexible non-null testing of aspheres and free-form surfaces with the tilted-wave-interferometer, Int. J. Optomech. 8 (2014) 242–250.
[12] X. Hou, F. Wu, L. Yang, Q. Chen, Experimental study on measurement of aspheric surface shape with complementary annular subaperture interferometric method, Opt. Express 15 (2007) 12890–12899.
[13] G. Baer, E. Garbusi, W. Lyda, W. Osten, Automated surface positioning for a non-null test interferometer, Opt. Eng. 49 (2010) 095602.
[14] J. Li, H. Shen, R. Zhu, Method of alignment error control in free-form surface metrology with the tilted-wave-interferometer, Opt. Eng. 55 (2016) 044101.
[15] Q. Hao, S. Wang, Y. Hu, H. Cheng, M. Chen, T. Li, Virtual interferometer calibration method of a non-null interferometer for freeform surface measurements, Appl. Opt. 55 (2016) 9992–10001.
[16] D. Liu, T. Shi, L. Zhang, Y. Yang, S. Chong, Y. Shen, Reverse optimization reconstruction of aspheric figure error in a non-null interferometer, Appl. Opt. 53 (2014) 5538–5546.
[17] L. Zhang, D. Liu, T. Shi, Y. Yang, Y. Shen, Practical and accurate method for aspheric misalignment aberrations calibration in non-null interferometric testing, Appl. Opt. 52 (2013) 8501–8511.
[18] L. Zhang, D. Liu, T. Shi, Y. Yang, S. Chong, B. Ge, Y. Shen, J. Bai, Aspheric subaperture stitching based on system modeling, Opt. Express 23 (2015) 19176–19188.
[19] TRIOPTICS, SpectroMaster. http://www.trioptics.com/spectromaster/description.php.
[20] C. Tian, Y. Yang, Y. Zhuo, Generalized data reduction approach for aspheric testing in a non-null interferometer, Appl. Opt. 51 (2012) 1598–1604.
[21] Form Talysurf i-Series. https://www.taylor-hobson.com.cn/products/surface-profilers/i-series-range/form-talysurf-i-series.